Sonic Boom Ground Noise Minimization Via the Adjoint Method

David L. Rodriguez[1]
Science & Technology Corp., Moffett Field, CA 94035

Michael J. Aftosmis,[2] Marian Nemec,[3] and Sriram Rallabhandi[4]
NASA Ames Research Center, Moffett Field, CA 94035

A multidisciplinary design optimization methodology to directly minimize the ground-level noise generated by the sonic boom of a high altitude supersonic body is presented. A Cartesian Euler flow solver is coupled with an atmospheric propagation tool to create a ground-noise analysis capability for supersonic bodies. Adjoint formulations for both the flow solver and propagation tool are also coupled to compute sensitivities of shape variations in the body in a highly efficient manner. A gradient-based optimizer is then introduced to forge a valuable design capability. Output-based mesh adaptation that is driven directly by ground-level noise is employed to increase accuracy and provide error estimation. The design method is demonstrated first on a simple axisymmetric body with few design variables to evaluate the efficacy of the optimization scheme. Guided by the results of this initial case, the problem is then repeated with somewhat different design variables to further demonstrate the capabilities of the design method. Finally, the method is applied to a real-world problem by optimizing control surface deflection settings of a low-boom aircraft to minimize ground noise while maintaining trimmed, level flight.

I. Nomenclature

$ASEL$	=	A-weighted Sound Exposure Level
B_n	=	Bernstein polynomial scale factor
C_M	=	aircraft pitching moment coefficient
h	=	cruise altitude
L	=	aircraft lift force
Q	=	`Cart3D` flow solution
p_{gs}	=	ground-level pressure signature
p_{ns}	=	near-field pressure signature
R_{max}	=	maximum radius of an axisymmetric body
T	=	tessellation of an outer mold line
X	=	generic geometry design parameters
α	=	angle of attack
δ_a	=	aileron deflection
δ_f	=	flap deflection
δ_s	=	stabilator deflection
δ_t	=	T-tail deflection

[1] Senior Research Scientist, Computational Aerosciences Branch; david.l.rodriguez@nasa.gov, Senior Member AIAA.
[2] Aerospace Engineer, Computational Aerosciences Branch; michael.aftosmis@nasa.gov, Associate Fellow AIAA.
[3] Aerospace Engineer, Computational Aerosciences Branch; marian.nemec@nasa.gov, Senior Member AIAA.
[4] Aerospace Engineer, Computational Aerosciences Branch; sriram.rallabhandi@nasa.gov, Associate Fellow AIAA.

II. Introduction

Increased commercial and national interest in overland supersonic flight has spurred tremendous progress in accurate sonic boom analysis and design. Effective methods have been developed for near-field sampling with CFD (Computational Fluid Dynamics) tools ranging from Euler to Reynolds-averaged Navier-Stokes solvers using unstructured and structured meshes [1-6]. In particular, output-based mesh adaptation, which exploits adjoint sensitivity formulations, has proven to be an enabling technology for sufficiently accurate near-field pressure signature predictions [7, 8]. Concurrently, atmospheric propagation tools have matured to the point where ground noise can be predicted within a decibel, even for low-boom aircraft designs [9-13]. When combined, these tools provide a powerful approach (depicted in Fig. 1) for the complete ground-level noise analysis of low-boom aircraft. The CFD solver is used to compute an accurate near-field pressure signature that is far enough from the aircraft to minimize complex, three-dimensional, aircraft geometry effects. This pressure signature is then processed by an atmospheric propagation tool to compute the raw ground-level acoustic signature. Finally, that raw signal is then appropriately weighted to compute ground-level noise metrics which represent what human beings actually hear.

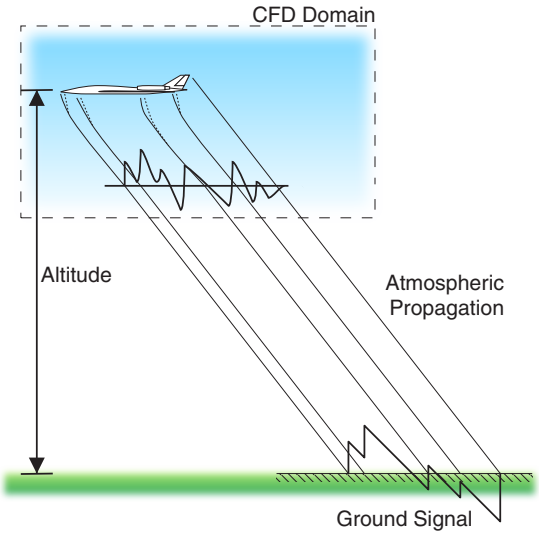

Fig. 1. Sonic boom prediction process.

While high-fidelity acoustic signature analysis has matured significantly, its applicability to design optimization has mostly been relegated to an inverse design process where the near-field pressure signature is proposed as a goal [14]. A CFD-based shape optimization method is then applied to an aircraft with the hope of actually producing this target pressure signature. While the signature is chosen so that it results in low ground noise, it can almost never be realized by an actual complex aircraft design. Likewise, an optimal target pressure signature is rarely apparent. Inverse design methods are really only productive when the optimal target is known ahead of time. Nevertheless, this technique has been shown to be effective in reducing ground-level noise of low-boom aircraft designs [14-18].

More recent work has begun to address direct minimization of ground-level noise metrics through shape optimization [19]. The work presented here expands upon those efforts by presenting the latest design optimization methods and applying them to a simple axisymmetric body. The first example presented uses a limited number of design variables, which allows the optimization results to be thoroughly validated with a detailed exploration of the design space. A second example that is inspired by the results of the first problem is also presented to further demonstrate the efficacy of the adjoint-based methodology.

The final example design problem presented involves an actual low-boom aircraft. A previously completed optimization [20] is revisited but with significantly improved gradients. At the time of publication, ground testing of the X-59 Low-Boom Flight Demonstrator (LBFD) [21] has begun with flight testing soon to follow. While the aircraft outer mold line is fundamentally frozen, avenues to lessen ground-level noise remain. The X-59 has four sets of control surfaces and at cruise is over-controlled, meaning that there are multiple combinations of surface deflections that still allow the aircraft to maintain trimmed, level, unaccelerated flight. The control surfaces also have an appreciable effect on the acoustic signature produced by the aircraft. This presents an opportunity to partially manage the ground-level noise of the aircraft by modifying control surface deflections and flight conditions. To further demonstrate its capability, the design optimization process discussed above is also applied to this real-world problem.

III. Methodology

To directly minimize the ground-level noise produced by a body flying at high altitude and supersonic speeds, a multidisciplinary design optimization (MDO) method was built using a set of already existing and well-validated tools. This set includes a parametric geometry generator, a CFD solver, an atmospheric propagation tool, and a numerical optimizer. Each tool and its role in the design method are discussed and presented below.

ESP [22, 23] is a constructive geometry creation and manipulation system specifically designed for building aerospace-related geometries. An open-source computer-aided design (CAD) geometry kernel is employed giving it

the capability to output geometry files compatible with most commercial CAD packages. **ESP** can also output tessellated outer mold lines [24] which are compatible with many CFD flow solvers, a capability that is fully exploited in the presented MDO method. Parametric geometry can be built allowing the user to rapidly modify a model by simply changing the values of user-defined design parameters. Sensitivities of the geometric model to these design parameters are also exposed to the user which is an attractive feature for shape optimization. These sensitivities can also be computed for the tessellated version of the geometry model, thus making **ESP** ideal for the MDO method in particular [25].

Cart3D [26] is an aerodynamics simulation package that solves the Euler equations on an adaptive Cartesian mesh. The user provides a watertight surface triangulation, and the solver generates a Cartesian mesh automatically using the cut-cell approach [27]. The package also includes an adjoint solver [28] which allows for both output-driven mesh adaptation [29] and sensitivity calculation [30]. **Cart3D** has proven to be excellent at computing accurate near-field pressure signatures which can be used to compute the acoustic signature of a vehicle [31, 32]. Another tool, **trix**, is provided in the **Cart3D** package which allows the user to rotate tessellated geometry components about arbitrary axes. In this work, **trix** is used to deflect the control surfaces of an already tessellated aircraft geometry.

The third tool used to minimize ground-level noise is **sBOOM** [10], which solves an augmented Burgers equation thus propagating a pressure signature from the cruise altitude through the atmosphere to the ground. The solver also incorporates an adjoint formulation that can compute the sensitivity of the propagated ground signature to the original pressure signature at altitude [33]. This capability is critical for both noise-driven mesh adaptation and gradient-based optimization. **sBOOM** also computes ground-level noise metrics from the ground signature, including the A-weighted Sound Exposure Level (*ASEL)* [34, 35]. Metrics like this transform the waveform of the ground signature into quantifiable measures of noise experienced by a human listener. The adjoint formulation of **sBOOM** also incorporates the noise metric computation, thus supplying the user with sensitivities of noise to the provided near-field pressure signature.

The final tool used in the MDO method is **SNOPT** [36], which uses a sequential-quadratic-programming (SQP) algorithm to perform gradient-based numerical optimization. **SNOPT** can handle both linear and nonlinear formulations of both the objective and constraints. The adjoint solvers incorporated in **Cart3D** and **sBOOM** are exploited to evaluate the gradients of any computed functions with respect to all design variables. For the direct minimization of noise from an acoustic signature, the objective function would naturally be the ground-level noise metric. Ground-level noise gradients with respect to geometry design parameters can be computed using the chain rule. For example, the gradient of *ASEL* with respect to a geometric design parameter (X) can be computed using Eq. (1):

$$\frac{d(ASEL)}{dX} = \frac{\partial(ASEL)}{\partial p_{gs}} \frac{\partial p_{gs}}{\partial p_{ns}} \frac{dp_{ns}}{dQ} \frac{dQ}{dT} \frac{dT}{dX} \tag{1}$$

where p_{gs} is the ground-level pressure signature, p_{ns} is the near-field pressure signature, Q is the **Cart3D** flow solution, and T is the geometry model tessellation. The gradient of *ASEL* with respect to the ground-level signature is provided by **sBOOM**, as is the gradient of the ground-level signature with respect to the near-field signature. **Cart3D** computes gradients of the near-field signature to the flow solution as well as that of the flow to the tessellation. Nemec et. al. [37] gives a detailed discussion of the **Cart3D-sBOOM** linearization. The gradient of the tessellation with respect to the design parameter is provided by **ESP** and/or **trix**.

While *ASEL* is nominally the objective function, constraints on the forces and moments acting on the aircraft are necessary for a realistic design problem. For example, if a constraint on the pitching moment coefficient is enforced, the gradient with respect to a geometry design parameter can be computed using Eq. (2):

$$\frac{dC_M}{dX} = \frac{\partial C_M}{\partial Q} \frac{dQ}{dT} \frac{dT}{dX} \tag{2}$$

where all of the terms are computed by **Cart3D** and perhaps **ESP** within the optimization framework [38]. For design problems involving boom propagation, exploiting cruise altitude as a design variable is often advantageous. Since **Cart3D** is an inviscid code, altitude actually only affects atmospheric propagation results. Theoretically, the required engine thrust should also be affected by changes in altitude, but for this work, the plume flow into the computational domain is assumed to be constant. Doing otherwise would require a propulsion analysis within the design method which is currently beyond the scope of this work. Thus, **sBOOM** alone must provide gradients of the

noise metric with respect to altitude as in Eq. (3):

$$\frac{d(ASEL)}{dh} = \frac{\partial(ASEL)}{\partial p_{gs}} \frac{dp_{gs}}{dh} \tag{3}$$

Eq. (1) represents a fully-coupled, multidisciplinary sensitivity calculation that combines near-field CFD, atmospheric propagation, and acoustic noise evaluation. Employing this approach with the tools already described, a fully-coupled, ground-level noise driven, design optimization method can be built using the architecture shown in Fig. 2. A typical design iteration begins with predicted values for geometry design parameters (which may include body shape, control surface deflections, and/or angle of attack) provided by **SNOPT** to **ESP** and **trix**. The geometry is accordingly built by **ESP** and perhaps control surfaces are deflected by **trix** to produce a new triangulation. **Cart3D** takes that new triangulation and generates an adapted volume mesh and solution. Forces and moments acting on the aircraft along with their gradients with respect to the design variables are fed back to **SNOPT**. The near-field pressure signature is extracted from the solution and passed to **sBOOM**. The altitude predicted by **SNOPT** is also passed to **sBOOM**. The ground pressure signature and corresponding ground-level noise metric are computed along with gradients and are passed to **SNOPT**. At that point, **SNOPT** uses the objective and constraint values and gradients to determine new values for the design variables that attempt to improve the ground noise while satisfying the constraints. Using the SQP algorithm, the process continues until a local optimum is discovered.

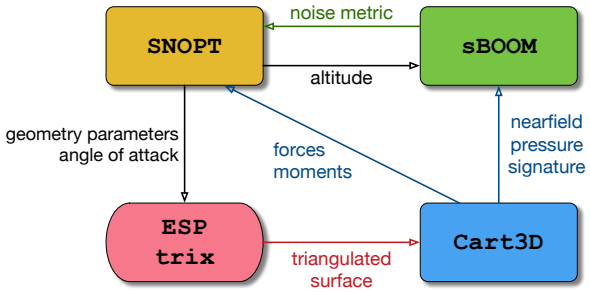

Fig. 2. Architecture of design optimization method illustrating values and their sensitivities passed between the coupled tools.

IV. Applications

The methods described in the previous section were applied to two geometries: a simple axisymmetric body and the Low-Boom Flight Demonstrator (X-59) [21] aircraft design. The simple body is used primarily to verify the method is working properly and provide a preliminary assessment of its capability. Two design problems are performed on this geometry and a thorough analysis of the results is presented. The final example represents a real-world problem: the sonic boom noise from the X-59 is reduced by identifying an optimized set of control surface deflections at cruise.

A. Axisymmetric Body - Problem 1

The first geometry the MDO method is applied to is an axisymmetric body. The body is 200 feet long and is constrained to have a maximum radius that is no less than 5 feet. These selected dimensions were based roughly on the fuselage of a Boeing N+2 low-boom aircraft (QEVC) design [39]. The geometry is constructed by first taking the axial radius distribution of a Sears-Haack body that has a maximum radius of 1.25 feet. Added to that thin baseline (fixed) body are radius distributions computed by three of the five 4th-order Bernstein polynomials that

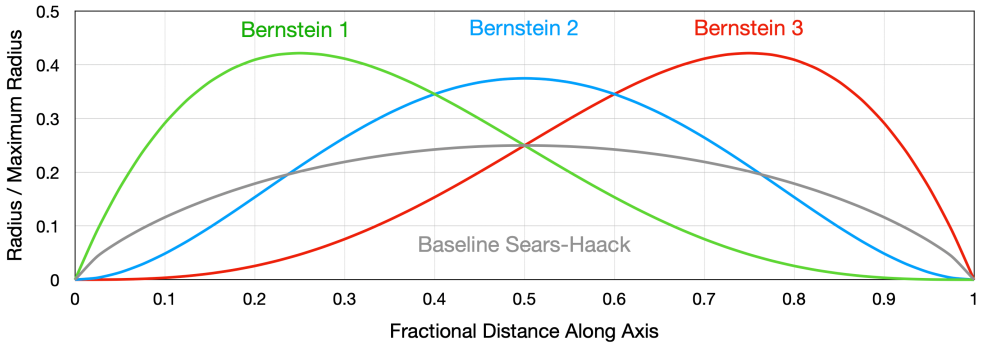

Fig. 3. Baseline radius distribution (grey) and Bernstein polynomials (green, blue, red) used to build parametrized axisymmetric body.

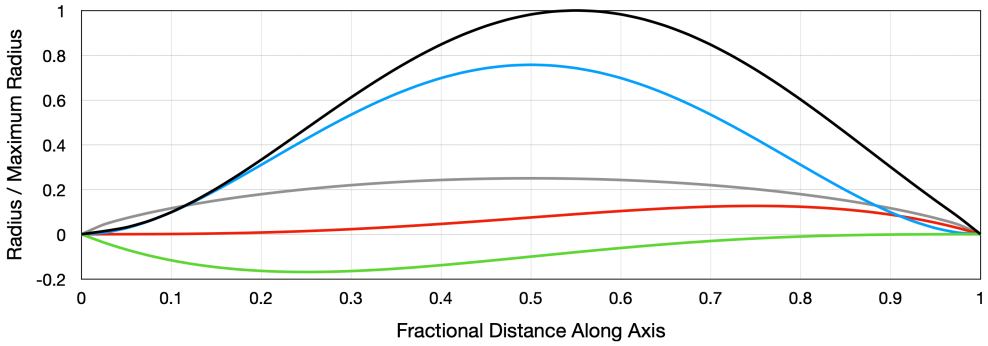

Fig. 4. Example radius distribution (black) built by superimposing the baseline shape (grey) and three individually scaled Bernstein polynomials (green, blue, red) from Fig. 3.

have peaks at 25%, 50%, and 75% of their lengths. The two polynomials with peaks at the ends are not included since they would eliminate the sharp nose and tail of the body. The baseline radius distribution (normalized by the constraint on maximum radius) and the raw Bernstein polynomials are shown in Fig. 3. The axisymmetric body of this problem is built by adding the radius distributions of the baseline Sears-Haack body and the Bernstein polynomials which each have a individual scale factor. In this construction, the body shape is parameterized by the scale factors for each Bernstein polynomial. An example normalized radius distribution is shown in Fig. 4. This parametrization allows for the front and back ends of the body to not get too sharp while permitting the axial location of the maximum radius to vary. Though the range of body shapes is ultimately limited because only three parameters can be varied, the body does lend itself to a very interesting design problem that can be easily verified.

For this small design problem, the discrete geometric model of the body is built using **`ESP`** for any specified set of Bernstein polynomial scale factors. This parametrized body is flown at Mach 1.5 and 55,000 feet of altitude at zero angle of attack. The objective is to minimize the ground level noise produced by this geometry as measured by the *ASEL* metric. Though the body maximum radius is constrained, the parametrization allows for the axial location of the peak radius to vary. The design variables are naturally the scale factors (designated B_1, B_2, and B_3) that are applied to the Bernstein polynomials shown in Fig. 3 to build up the body radius distribution. Eq. (4) summarizes the optimization problem:

$$\begin{aligned} \text{minimize:} \quad & ASEL\,(B_1, B_2, B_3) \\ \text{subject to:} \quad & R_{max} \geq 5 \text{ feet} \end{aligned} \tag{4}$$

The optimization problem was run using the MDO method presented in Fig. 2. The computational meshes employed had over 100 million cells over the entire domain (no symmetry plane) and were generated using output-

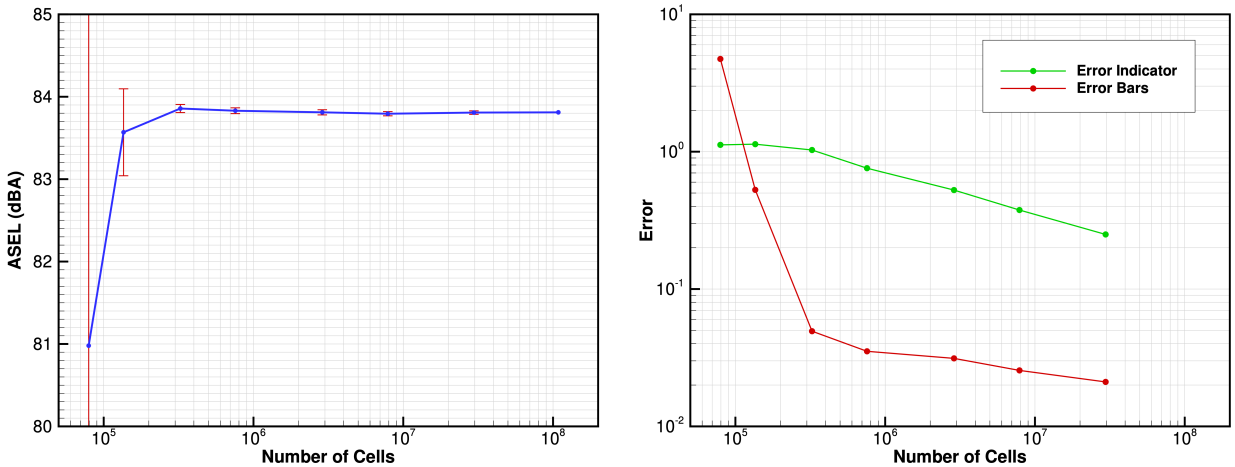

Fig. 5. Functional convergence and error reduction as the mesh is adapted for a typical analysis cycle in design of the axisymmetric body in Fig. 3.

based adaptation. The design objective, *ASEL*, was also the functional used to drive the adaptation. A typical analysis is represented in Fig. 5. The left plot shows the convergence of the functional (*ASEL*) as the mesh is adapted. The right plot shows the reduction in both the error indicator, which is used to drive the adaptation of the mesh, and the estimated error bar size surrounding the value of the functional. This error range is also shown in the functional history in the left plot. Both plots show excellent convergence of the *ASEL* functional which indicates the final value is accurate at least to about a tenth of a decibel. A typical final mesh generated by this analysis is shown in Fig. 6, colored by cell size.

In fact, the value of the functional was nearly converged after just a few adaptation cycles, but the adaptation

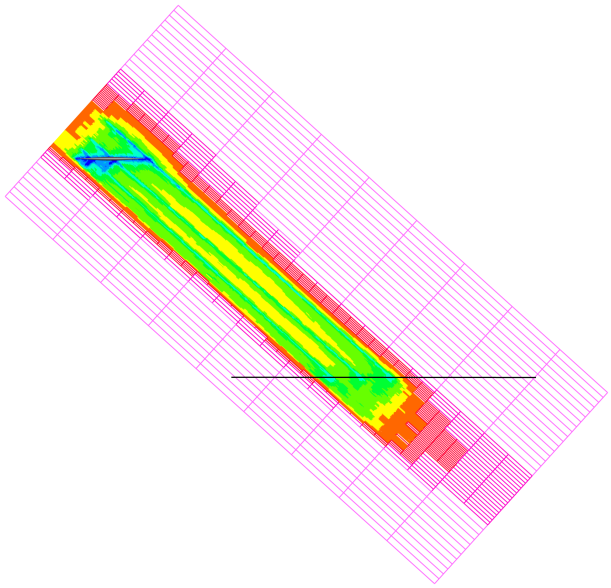

Fig. 6. Planar cut of a typical finest adapted mesh on axisymmetric body. Cells are colored by refinement level, with reds being the coarsest and blues the finest. The body is shown in grey at the top. The nearfield pressure sensor is indicated by the black line.

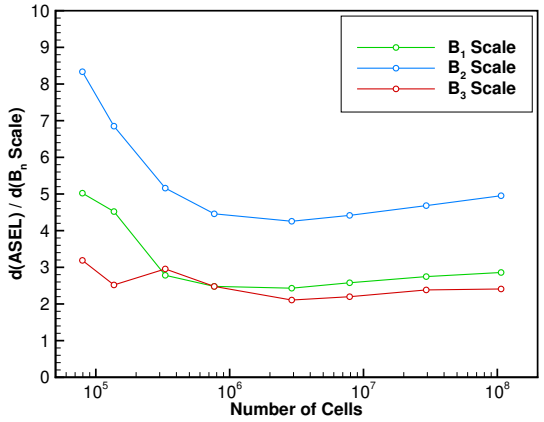

Fig. 7. Convergence of design variable gradients with adapted mesh size.

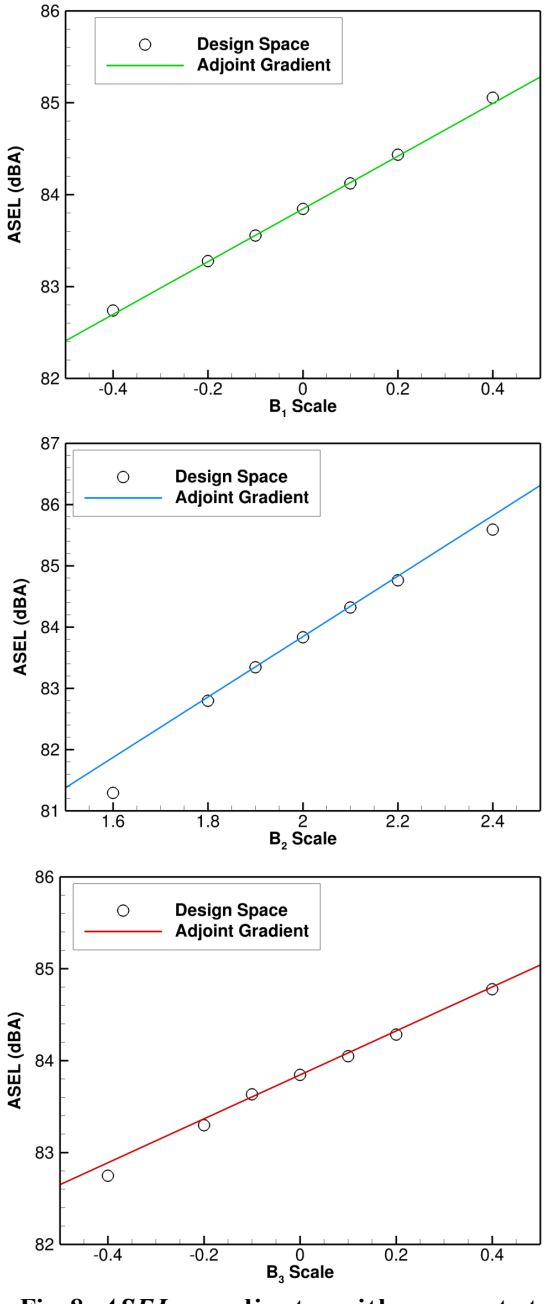

Fig. 8. *ASEL* gradients with respect to Bernstein polynomial scales as computed by coupled adjoint solver. They are compared to samplings of the actual design space.

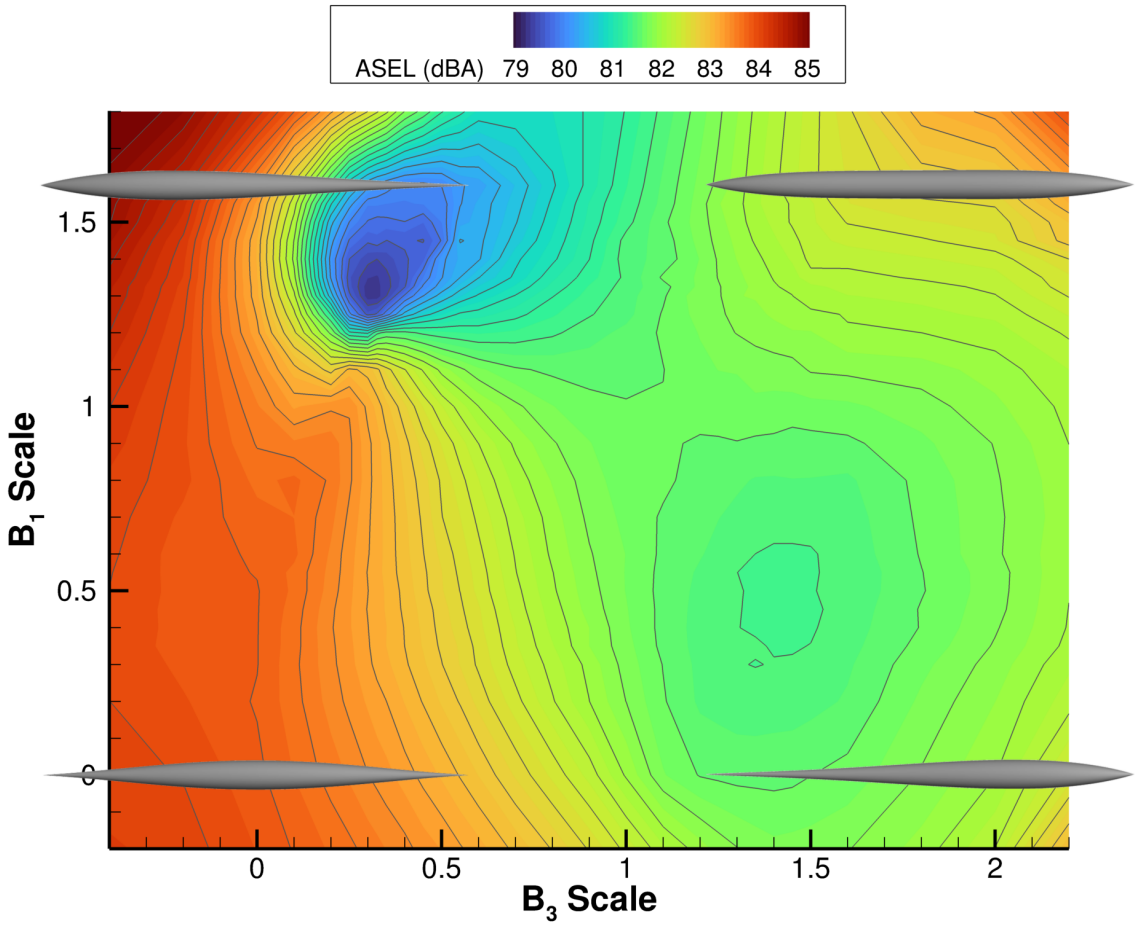

Fig. 9. *ASEL* design space of axisymmetric body, constrained in B_2 scale to match radius constraint.

process was continued to ensure that the design variable sensitivities, which are computed using the adjoint solution, were also accurate. Fig. 7 shows the computed gradients of *ASEL* with respect to the design variables at each adaptation cycle (mesh size). The plot shows that not all the gradients are completely converged, but they do appear to be reasonably close. Fig. 8 graphically shows these partial derivatives and compares them to a sampling of the design space varying only one variable at a time. The computed gradients show quite excellent accuracy. All of these results suggest that the coupling of **`Cart3D`** and **`sBOOM`** is indeed sound and could produce positive results in a gradient-based optimization setting, assuming the design space is smooth, of course.

Since this design problem has three design variables with one constraint, it is possible to make a two-dimensional plot of the constrained design space. Fig. 9 is an example of such a plot. Here, the two dimensions are the scale factors of the 1st and 3rd Bernstein polynomials (see Fig. 3). The 2nd Bernstein scale factor is constrained to whatever value gives the axisymmetric body a maximum radius of exactly 5 feet. The contours show *ASEL* values throughout this design space. Examples of the body shape are shown in several locations of the space for clarity. The contour plot was constructed by completing 780 analyses sampling the range of space presented. The design space is fascinatingly multimodal. In hindsight, this is to be expected since the ground pressure signal is formed after the coalescing of multiple shocks which occurs as they propagate through the atmosphere. What may not have been expected is that the design space is relatively smooth. This feature should make gradient-based optimization not only possible but effective, though it certainly will not guarantee a global minimum will be found.

Fig. 10. Baseline and optimized geometries (first run).

After exploring the design space and

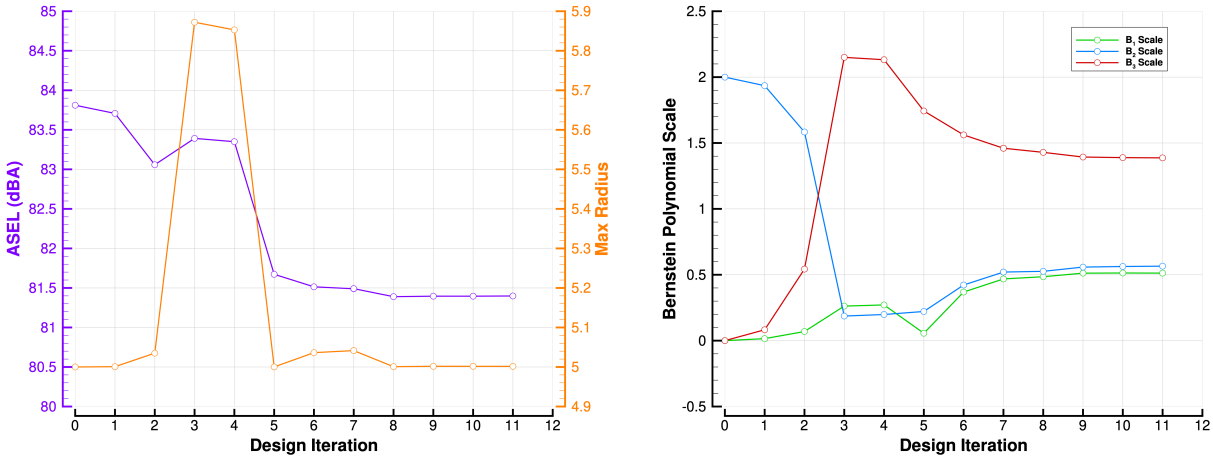

Fig. 11. Optimization history (first run) of axisymmetric body. Objective and constraint are shown on the left with the design variables on the right.

verifying the gradients computed by the coupled MDO method, two optimization problems were attempted at different starting points. For the first run, the initial design started with both the B_1 and B_3 scale factors set to zero and the B_2 scale factor set to 2.0, which builds a geometry that satisfies the radius constraint exactly and is symmetric front to back. This geometry is shown as the baseline geometry in Fig. 10. The results of the optimization are shown in Fig. 11. The objective function (*ASEL*) is shown to be reduced to a value over 2 dB below the initial value. The maximum radius constraint is also satisfied by reaching the constraint exactly at 5.0 feet. The optimized geometry is shown in Fig. 10. Both the nose and back end have become much blunter, and the location of the maximum radius has moved back to roughly 59% of the body length. This corresponds to the local minimum shown in Fig. 9 in the lower-right portion of the sampled design space.

But as was shown in Fig. 9, the design space is multi-modal; there is another local minimum that indeed appears to be much better than this first solution. Hence, the optimization was repeated with a different starting point in hopes of locating this second and indeed global minimum. The starting geometry for this problem is shown in Fig. 12. The resulting optimization history is shown

Fig. 12. Baseline and optimized geometries (second run).

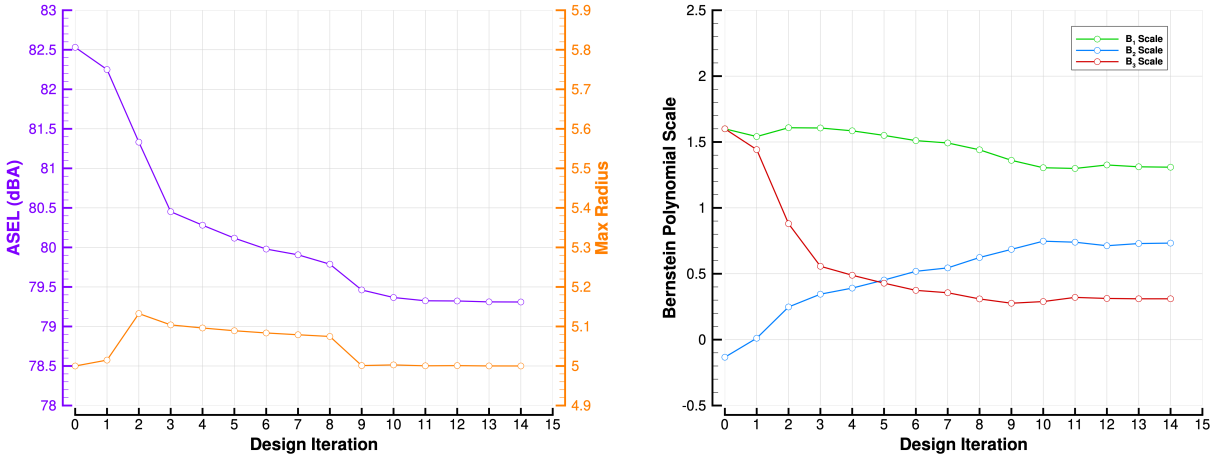

Fig. 13. Optimization history (second run) of axisymmetric body (take 2). Objective and constraint are shown on the left with the design variables on the right.

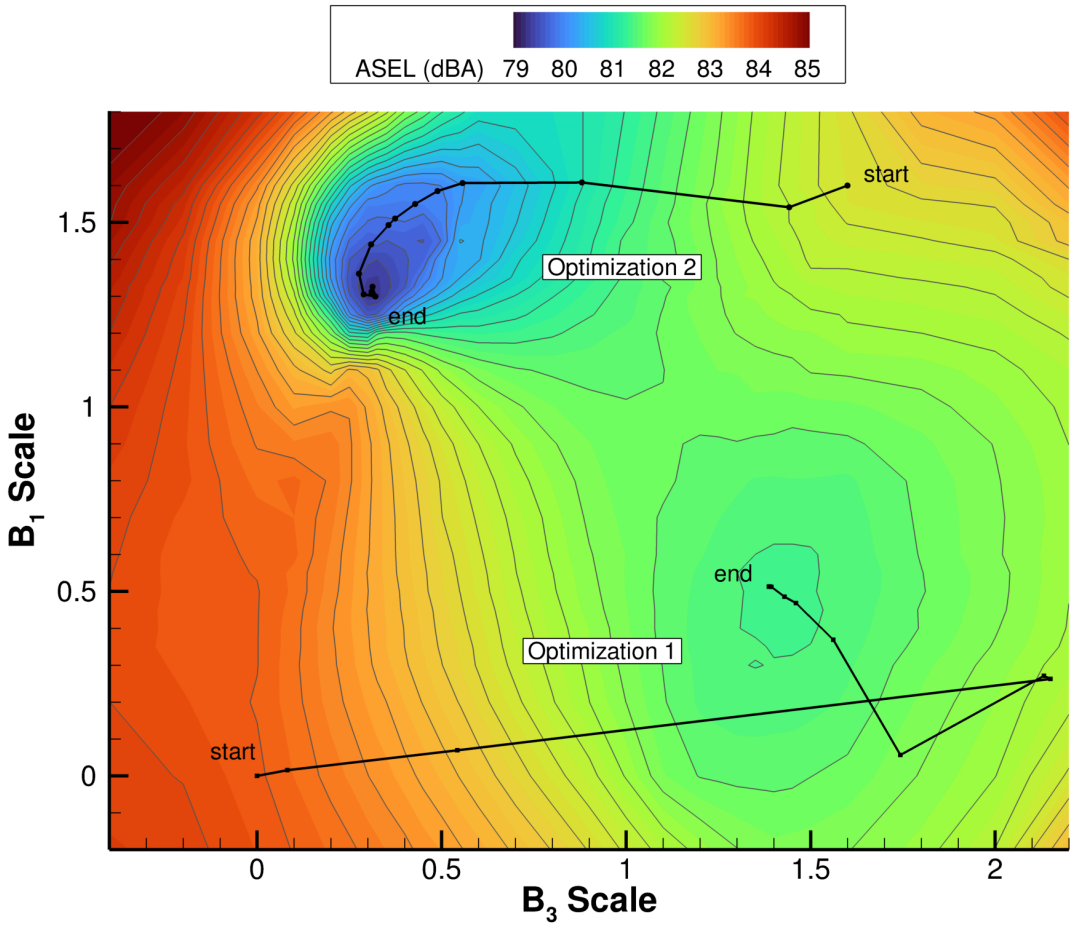

Fig. 14. Optimization trajectories projected onto constrained design space. Note the actual trajectories only lie on this surface near the optima (and starting points).

in Fig. 13 indicating another optimum was found that is over 2 dB quieter than the first optimized solution while still satisfying the constraint. The resulting optimized geometry is shown in Fig. 12, which is quite different than the optimized geometry in Fig. 10. Here the maximum radius has moved *forward* of the midpoint to roughly 37% of the body length.

The optimization trajectories are shown in Fig. 14 as projections onto the design space of Fig. 9. Note that these trajectories do not actually lie entirely on this surface since the constraint is not satisfied at every design cycle but only near the end where the optima are located. These projected trajectories behave as is expected by a constrained SQP method. Both trajectories end at or very near the optima identified in the design space sampling. These results demonstrate that the MDO method is indeed capable of locating local minima in what seems to be a smooth, though multimodal, design space. These results also show that while gradient-based optimization is possible and even effective in these types of noise minimization problems, it does not guarantee that a global minimum can be discovered with just any starting point.

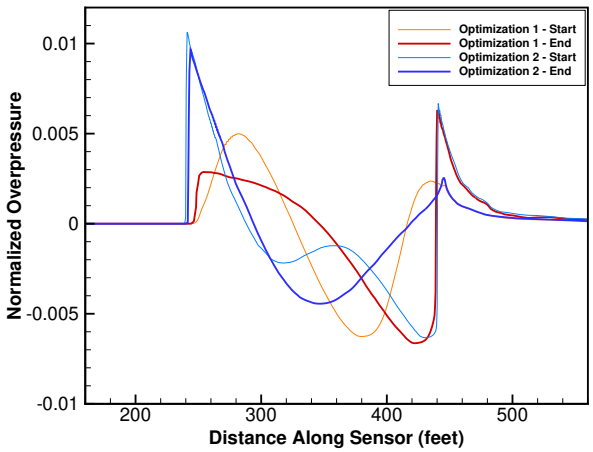

Fig. 15. Near-field pressure signatures of the starting and optimized (end) axisymmetric geometries.

Fig. 15 shows the near-field signatures for both the starting and optimized geometries analyzed. Naively, one would think the signature at the start of optimization 1 (orange) would produce the quietest ground signal. And yet, referring back to Fig. 14, it is actually the loudest of the bunch. This is further evidence that prescribing a near-field pressure signature for inverse design is not straightforward.

The corresponding ground pressure signatures are shown in Fig. 16. The ground signatures are nearly N-waves for all geometries. The first optimized ground signature (red) has a softer and rounded peak up front along with a slightly weaker shock in the back when compared to the starting signal (orange). This explains the reduction in noise for the first optimization. The aft shock on the second optimized signal (blue) has a longer rise time than the starting signal (cyan), which explains its reduction in noise.

Referring back to Fig. 16, it is not clear why the resulting noise level from the second optimization is so much lower than the first one. To explain this difference, a noise buildup analysis in both the forward and backward directions was conducted on both optimized ground pressure signals. The results are shown in Fig. 17. The backward buildup of the first optimized signal (dotted red) shows the noise is dominated by the aft shock, which is unsurprising considering the signal shape. On the other hand, the forward buildup of the second optimized signal (solid thick blue) shows that signal is dominated by the front shock, also as expected. These buildups show that the aft shock of the first optimized signal is much stronger than the forward shock of the second optimized signal. Revisiting Fig. 16, this becomes more apparent as the jump in pressure at the front shock of the second optimized signal is smaller than that of the aft shock of the first optimized signal.

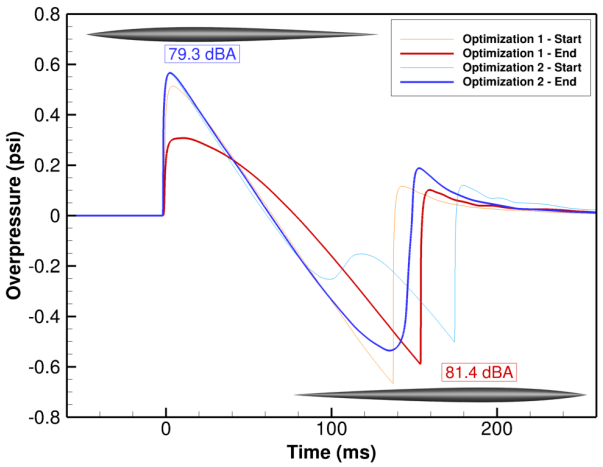

Fig. 16. Ground pressure signatures for baseline and optimized axisymmetric geometries. Optimized geometries and noise also shown.

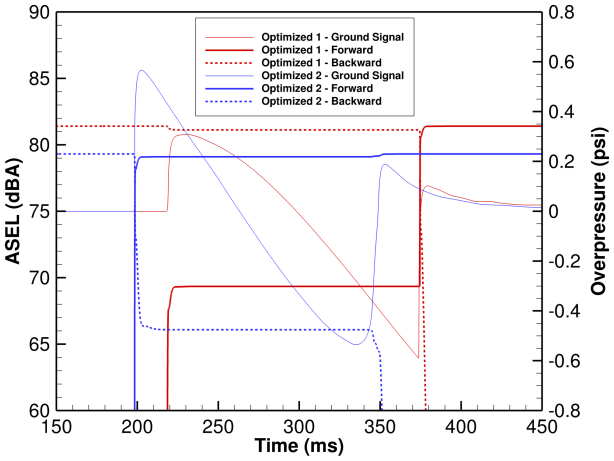

Fig. 17. Noise buildups (forward and reverse) of the optimized ground pressure signatures.

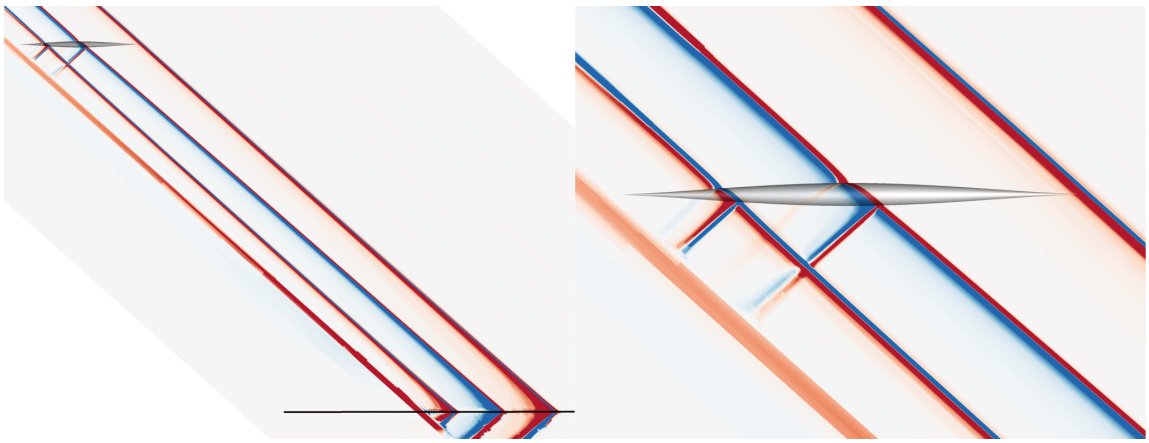

Fig. 18. Contours of pressure adjoint of *ASEL* from solution on axisymmetric body. Left image shows contours between body and line sensor (dark line). Right image is a zoom into the body itself. Red and blue contours indicate far from zero values.

B. Axisymmetric Body - Second Problem

A deeper dive into the first problem above yields another interesting design problem. Consider the baseline symmetric geometry shown in Fig. 10. Contours of the *ASEL*-adjoint of the pressure variable on the symmetry plane are shown in Fig. 18. Note the prominent spikes in the contours that intersect at roughly 26% and 57% of the body length. Since the adjoint contours directly illustrate the sensitivity of *ASEL* noise, these indicate that the shape of the body at these limited locations should have a significant effect on the ground noise level.

This observation prompted the authors to consider a second problem on the axisymmetric body. Here the baseline geometry is the same as in Fig. 10, but instead of modifying the radius distribution along the entire length of the body, only the radii at the locations of the adjoint spikes are allowed to vary. Radii in front, between, and back of these locations are held constant. Since the geometry is built by smoothly lofting a stack of circles along the length of the body, varying the radii exclusively at these locations amounts to creating small, smooth bumps or divots. Thus a new, two-variable problem is identified with no constraint necessary since the maximum radius value and location are fixed at the midsection. An example geometry with these two radii varied in an exaggerated fashion is shown in Fig. 19. Note the geometry is also scaled by a factor of two in the vertical direction for clarity.

The minimization of *ASEL* was repeated with changes in these two radii values as design variables (positive is a bump, negative a divot). Two different starting points were used since a prior exploration of the design space again suggested two local minima. The results of the first optimization are shown in Fig. 20. The design problem converged rather quickly and shows a reduction in noise of less than half a decibel. The front bump scale is minuscule and the aft bump is quite small (and positive). This result suggests these bumps might not be very effective at reducing noise.

The results of the second optimization, shown in Fig. 21, are quite different. This case also converged though it took several more iterations to do so. Starting with very small divots in both locations yielded an optimized design that is well over a full decibel quieter in *ASEL*. Again the front divot is mostly zeroed out, but the aft divot has become somewhat larger than the starting divot.

The optimization trajectories for both designs are shown in the sampled design space plot in Fig. 22. Note that the optimizations successfully located the two local minima. The design space shows that the forward bump as parameterized is essentially optimal when it is nearly zero. The aft bump, on the other hand, clearly can be used to reduce ground noise. The ground pressure signals induced by the baseline and optimized geometries are shown in Fig. 23. The baseline is the same as the baseline signal for optimization 1 in Fig. 16; it is essentially an N-wave. The optimized signals each show some deviation from the pure N-wave in the region in front of the second shock. These deviations are the source of noise reduction.

Fig. 19. Bump/divot design variables modeled on axisymmetric body as compared to baseline (vertical scaled by 2).

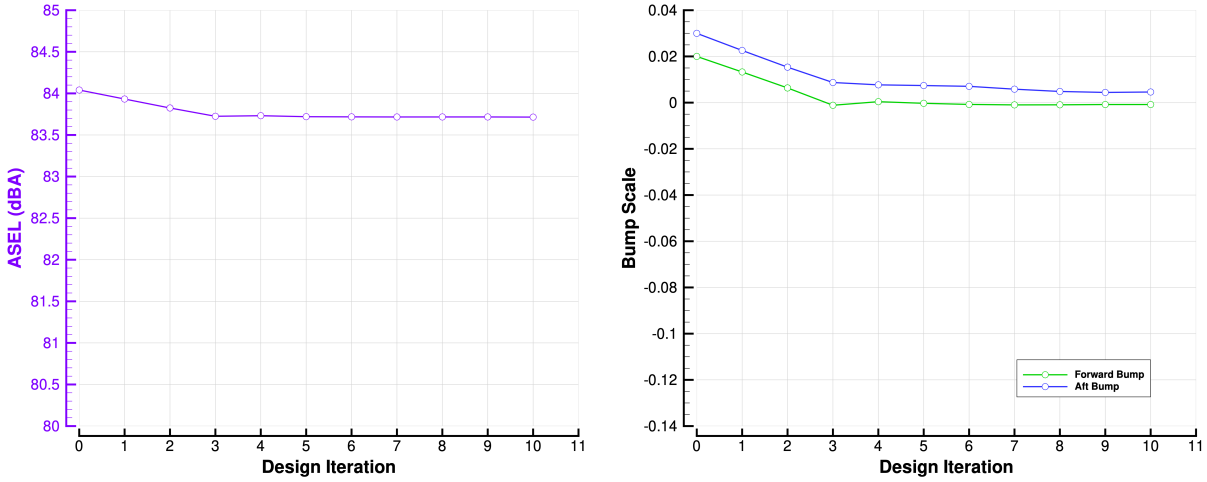

Fig. 20. Optimization history (first) of axisymmetric body with local bumps as design variables. Objective is shown on the left with the design variables on the right.

Overall, this optimization problem demonstrated that the adjoint solution produced by a ground noise based adaptation analysis can be used to identify potential design parameters. It showed that small divots on a simple axisymmetric body can have a significant effect on the ground noise. Of course, such a divot is only effective on a specific shape, at a specific Mach number, and a specific altitude. Even the aft divot probably would not be effective if the flight condition deviated from the optimized case. Such a divot would not be practical on an actual aircraft that must be low-boom throughout its supersonic flight envelope. Nevertheless, this problem did provide another excellent example of ground-based noise minimization through shape gradient-based optimization and verified the efficacy of the design method.

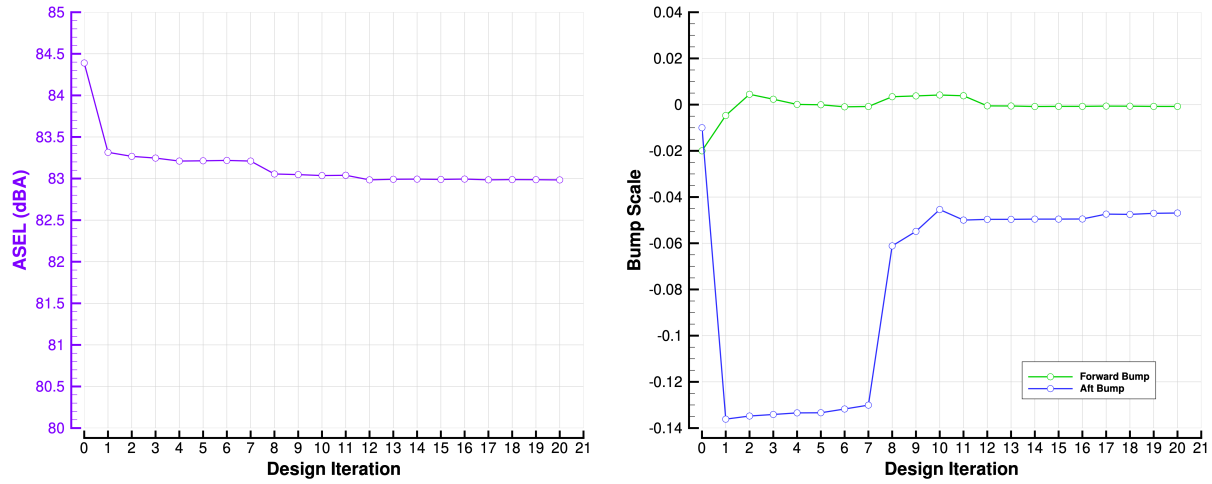

Fig. 21. Optimization history (second) of axisymmetric body with local bumps as design variables. Objective is shown on the left with the design variables on the right.

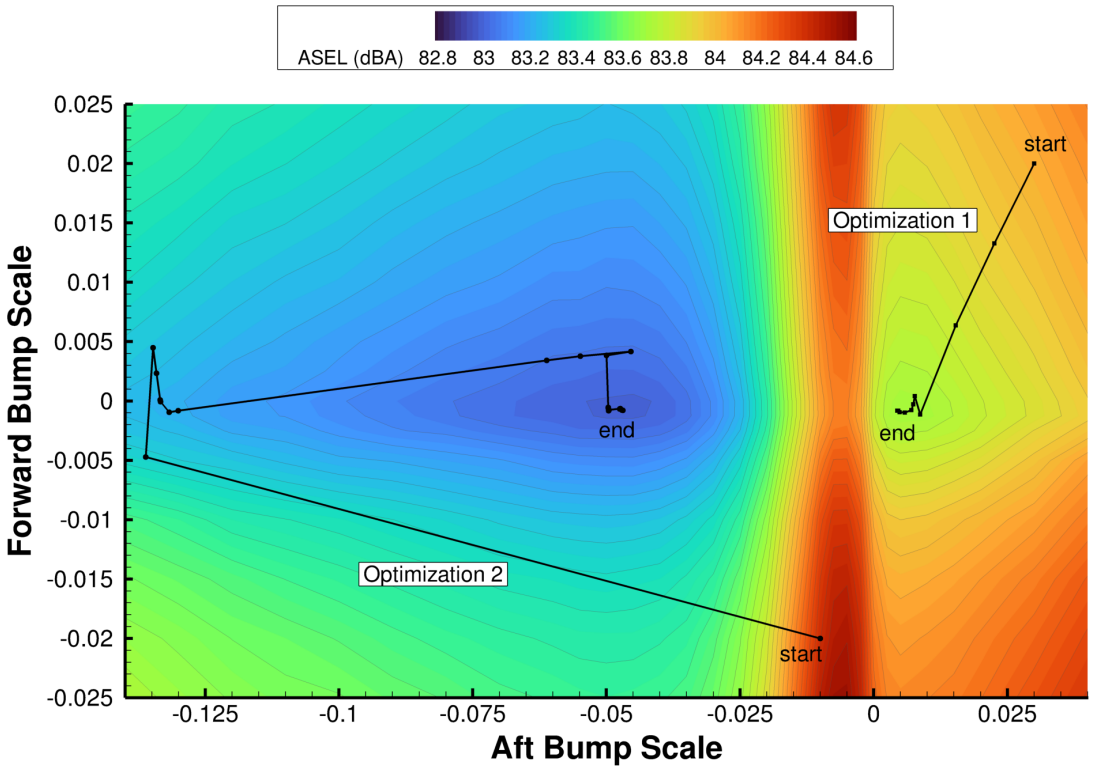

Fig. 22. Bump/divot optimization trajectories plotted in sampled design space.

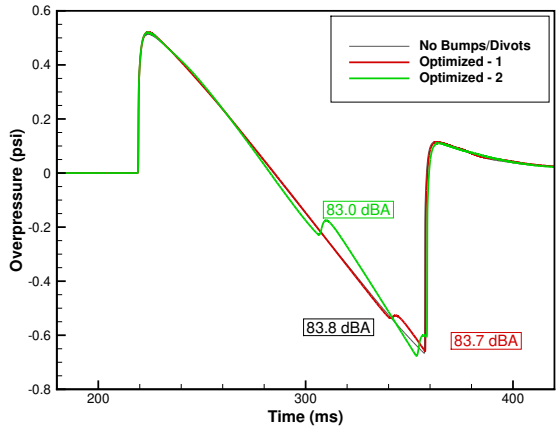

Fig. 23. Ground pressure signals from baseline and optimized bodies.

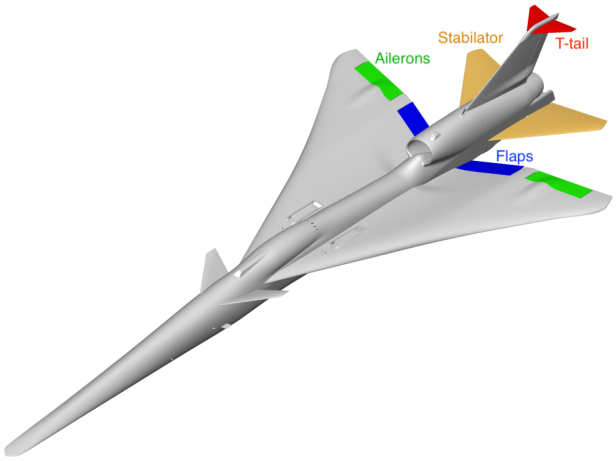

Fig. 24. X-59 aircraft with highlighted control surfaces.

C. Minimize X-59 Noise at Cruise

The final test case considers noise minimization of the X-59 aircraft via control surface deflections. As mentioned earlier, no changes to the outer mold line of the X-59 are possible at this time. But the aircraft is over-controlled and can fly most stable trajectories using many different settings of the control surfaces. These control surfaces are highlighted in Fig. 24. This presents an opportunity to optimize the control surface deflections for a specified objective, thus providing a real-world problem for the MDO method on a complex, low-boom aircraft design.

One such problem is to minimize ground noise due to sonic boom at cruise at a fixed lift, identical to the problem solved in [20]. The typical X-59 mission does not require fixed altitude in the cruise segment and thus altitude can vary along with the control surface deflections. This optimization problem can be summarized in Eq. (5):

$$
\begin{aligned}
\text{minimize:} \quad & ASEL\,(\alpha, \delta_f, \delta_a, \delta_s, \delta_t, h) \\
\text{subject to:} \quad & L\,(\alpha, \delta_f, \delta_a, \delta_s, \delta_t, h) = L_{cruise} \\
& C_M(\alpha, \delta_f, \delta_a, \delta_s, \delta_t, h) = 0 \\
& \delta_{f,min} \le \delta_f \le \delta_{f,max} \\
& \delta_{a,min} \le \delta_a \le \delta_{a,max} \\
& \delta_{s,min} \le \delta_s \le \delta_{s,max} \\
& \delta_{t,min} \le \delta_t \le \delta_{t,max} \\
& h_{min} \le h \le h_{max}
\end{aligned}
\tag{5}
$$

Note that in addition to the constraint on lift, a pitching moment constraint is enforced to ensure longitudinal trim. Since the control surface deflections are free to vary, maintaining trim is critical to a realistic design problem. These deflections are always identical on each side of the airplane.

While this problem is identical to that solved in [20], the difference here is in the design methods employed. The previous application used output-based adaptation driven by the near-field signature, while here the ground noise metric itself is used to refine the mesh. This was expected to improve the accuracy of the objective and gradient computation as was shown in [37]. Also, there have been tremendous improvements to **`sBOOM`** since this problem was initially tackled which resulted in vastly more accurate sensitivities [40, 41]. The gradient inaccuracies discovered in [20] were vastly reduced due to these improvements to **`sBOOM`**.

The version of the **`sBOOM`** tool used in this work (**`v2.9.1`**) does not provide gradients of the noise metrics with respect to altitude. Such a feature is under development, but until it is available, a model of the effects of altitude on ground-level noise has been created as a surrogate to close the design problem. Fig. 25 presents a plot of ground-level noise (*ASEL*) as a function of altitude for a fixed near-field pressure signature very similar to that produced by the X-59 at cruise. Note that the curve is nearly linear. This greatly simplifies the problem of the missing gradient of

noise with respect to altitude. For this work, this gradient is assumed to be constant and hence the slope of a line fitted through the curve in Fig. 25. In practice, the altitude provided to **sBOOM** is fixed and then the computed ground-level loudness is adjusted for actual altitude using this constant gradient. This simple model should work for small changes to the design and flight conditions. However, when large changes to the pressure signature are expected, it is preferable to obtain these gradients directly from the atmospheric propagation code.

One of the more current revisions (C612A) of the X-59 geometry was used for this optimization problem. As a reference, what is currently considered to be the best cruise flight condition (lowest ground noise) by the X-59 program is listed below in Table 1 as the nominal condition. Bounds for the deflections and altitude which stem from the vehicle's flight envelope are also provided. This represents the range of the design space that is considered in the optimizations presented below.

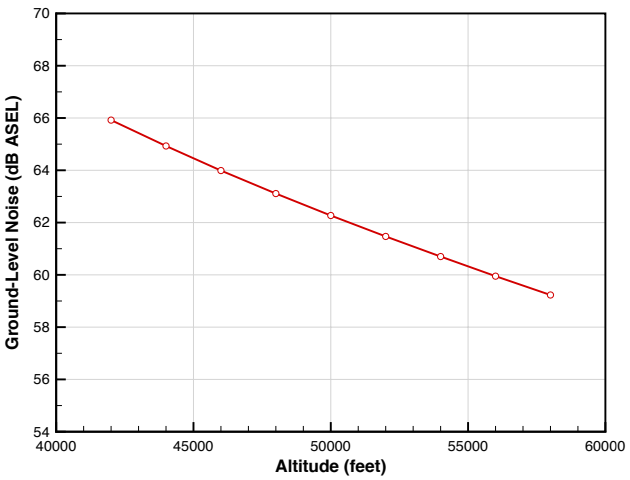

Fig. 25. Variation of *ASEL* ground-level noise metric as a function of altitude for a fixed near-field pressure signature.

Table 1. Control surface deflection bounds and nominal values used in design optimization.

Design Variable	Nominal	Minimum	Maximum
Ailerons	1.1°	-3.0°	3.0°
Flaps	-2.4°	-3.0°	3.0°
Stabilator	3.42°	-15.0°	15.0°
T-tail	3.7°	0.0°	10.0°
Angle of Attack	2.09°	-	-
Altitude (feet)	53,200	52,000	54,000

Output-based mesh adaptation was used for all analyses generated on the aircraft in the design optimizations. Body-axis-aligned volume meshes with roughly 23 million cells were used to compute forces and moments on the full span of the aircraft. The aircraft forces were used as the functional for adapting these meshes. Stretched, Mach-wave-aligned adapted meshes ranging from 150-230 million cells were used to compute the near-field pressure signature three body lengths below the aircraft. These solutions were conducted using only half the span of the airplane while exploiting the symmetry plane to conserve computational resources. Note that these meshes were significantly larger than those used in [20], almost by an order of magnitude. The ground noise metric, *ASEL,* served as the adaptation functional. Note these meshes on the very complex X-59 are only roughly double the size of the meshes used for the very simple axisymmetric body in the previous problems. Even though these were only half-span meshes (unlike the meshes on the axisymmetric body which modeled the full domain), the meshes used for the X-59 are relatively coarse; they are only double the size of those use for the simple axisymmetric body. These coarser meshes are used due to constraints on computational resources, thus surrendering some accuracy in the objective function and its gradient.

Referring back to the nominal condition listed in Table 1, the coupled **Cart3D-sBOOM** analysis of this case in a standard atmosphere predicts an *ASEL* of 63.7 dBA. At this angle of attack and altitude (assuming a standard atmosphere), the aircraft generates the required lift for level flight and is very nearly trimmed. The first optimization attempted used this nominal condition as a starting point. The method immediately stalled and failed to find a better design condition. Either additional mesh refinement is needed to improve accuracy, or the nominal state is indeed in the region of a local minimum. Further exploration of the design space in the region would be necessary to verify either hypothesis. Establishing this state as a nominal baseline, two additional optimizations were completed with two different starting conditions. These are listed in Table 2. Notice that Case 1 is quite far from the nominal state, while Case 2 is much closer.

Table 2. Initial X-59 control surface deflection values.

Design Variable	Case 1	Case 2
Ailerons	0.0°	1.5°
Flaps	0.0°	-2.0°
Stabilator	3.0°	3.0°
T-tail	0.0°	4.0°
Angle of Attack	2.3°	2.25°
Altitude (feet)	53,200	53,200

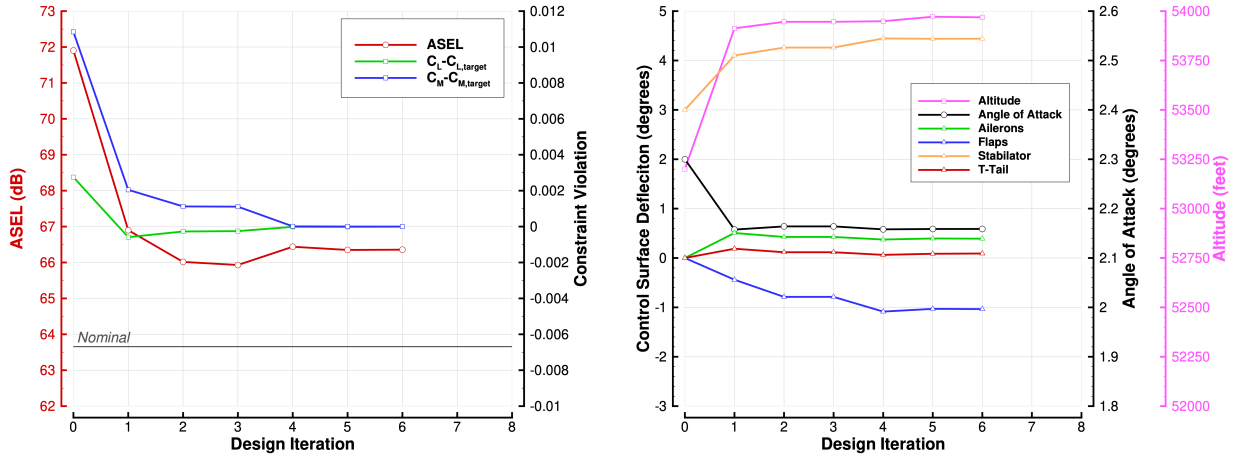

Fig. 26. Optimization history (Case 1) of X-59 with control surface deflections, altitude, and angle of attack as design variables. Objective (*ASEL*) and constraint violations (lift and moment) are shown on the left with the design variables on the right. The ground noise for the nominal case is also shown.

The optimization results for Case 1 are summarized in Fig. 26. The initial condition was comparatively loud at almost 72 dBA and the aircraft was far from trimmed. After 6 design cycles, the ground noise has been reduced to 66.4 dBA, the lift matches the weight, and the aircraft is trimmed. This optimization stalled after the 6 design cycles and attempts to restart from this final design failed to find a better flight condition. Again, this could be due to one of two reasons: either the design has reached a true local minimum, or additional mesh refinement is necessary to navigate the design space. Nevertheless, the optimizer was able to reduce ground noise over 5 decibels and achieve trimmed cruise. However, it was not able to produce a condition that was even at least as good as the nominal case which is still over 2 dBA quieter.

The ground signals for the initial, optimized, and nominal cases are shown in Fig. 27. The optimized signal shows a slightly lower peak up front due to the reduced angle of attack. But the major difference is the significant weakening of the rear shock which is the primary source of noise reduction. Comparing the optimized and nominal signatures reveals why the nominal case is still quieter. While the pressure jump for the aft shock is

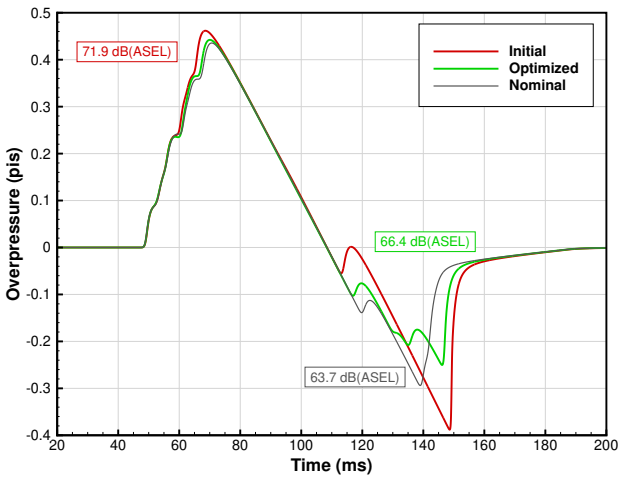

Fig. 27. Ground pressure signals from initial, optimized, and nominal conditions of the X-59 (Case 1).

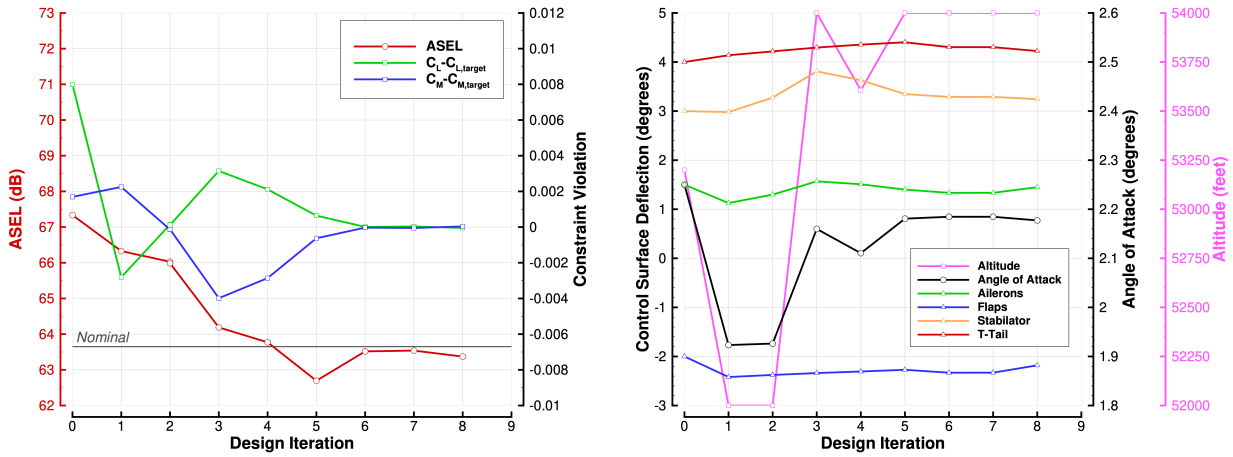

Fig. 28. Optimization history (Case 2) of X-59 with control surface deflections, altitude, and angle of attack as design variables. Objective (*ASEL*) and constraint violations (lift and moment) are shown on the left with the design variables on the right. The ground noise for the nominal case is also shown.

lower for the optimized case, the rise time of the nominal case is longer, which is the primary reason it is quieter.

The results for Case 2 which started much closer to the nominal condition are shown in Fig. 28. The initial condition is a little over 3 dBA louder than the nominal condition. The aircraft is also producing too much lift and is not trimmed. After 8 design cycles, the aircraft lift is now correct for cruise and the aircraft is trimmed. Also, the ground noise has been reduced to 63.4 dBA, which is a bit lower than that of the nominal condition. Looking at the ground signature comparison in Fig. 29, it is clear why. Both signatures are similar, particularly near the aft shock. However, the aft shock of the optimized signal is somewhat weaker. The slightly higher angle of attack of the optimized case produces a slightly higher peak of the front shock which should produce more noise. However, the optimized altitude has hit the maximum limit, which helps mitigate this increase in noise.

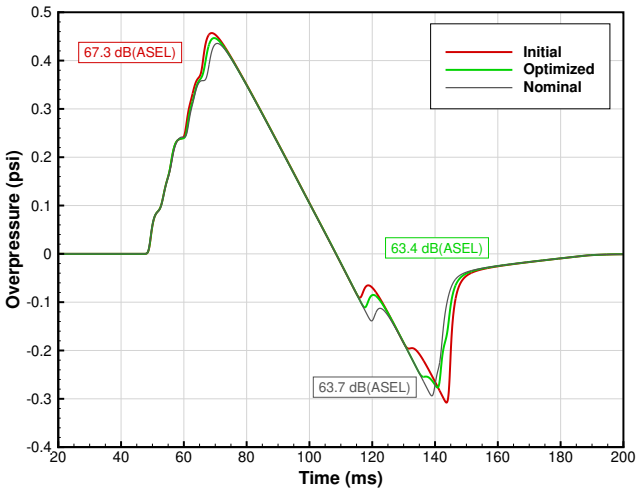

Fig. 29. Ground pressure signals from initial, optimized, and nominal conditions of the X-59 (Case 2).

The nominal and optimized conditions for both Case 1 and 2 are shown below in Table 3. Clearly the optimized Case 1 condition remains far from the nominal case, further suggesting a local minimum may have been located. Looking at Case 2, it is clear that all design variables (except the T-tail deflection) have moved closer to the nominal condition from the initial state listed in Table 2. Note that even though deflections are listed to the hundredth of a degree, operationally it may not be possible to set some of these surfaces to that degree of accuracy. However, the fact that both the nominal and optimized conditions result in similar ground noise suggests that they both may lie in a region of the design space near a local minimum. Thus, these results bode well for the success of the X-59 program, as there is a reasonably sized region of the flight envelope that produces what has been identified as the lowest ground noise level so far.

Comparing these two optimizations to the one presented in [20] shows that the method has become somewhat more efficient, reaching optima in less than 10 design cycles where several more design cycles were required before. Also, good results using the previous version of the method were difficult to achieve, whereas the current version of

the method is very often successful. There are many reasons for this improvement in performance, though the accuracy in the gradients is likely the predominant reason. Better gradients are the result of not only larger meshes that are adapted for the objective itself, but also the improvements in **sBOOM** detailed in [40].

Table 3. Optimized and nominal control surface deflection values for the X-59.

Design Variable	Nominal	Optimized (Case 1)	Optimized (Case 2)
Ailerons	1.1°	0.39°	1.44°
Flaps	-2.4°	-1.03°	-2.18°
Stabilator	3.42°	4.44°	3.24°
T-tail	3.7°	0.09°	4.22°
Angle of Attack	2.09°	2.16°	2.18°
Altitude (feet)	53,200	53,969	54,000

V. Conclusions

An improved version of a multidisciplinary design optimization tool that directly minimizes ground-level noise due to a supersonic aircraft has been presented. The method successfully couples a Cartesian Euler flow solver with an improved atmospheric propagation tool with built-in noise metric calculation. Adjoint solvers for both the flow solver and propagation tool have proven to be enabling technologies. The coupled adjoint solver has been successfully applied to output-based mesh adaptation where the functional of interest is the ground-level noise itself. This allows for more accurate computation of not only the noise level, but also any desired sensitivities. Using the coupled adjoint solver to compute ground noise sensitivities to user-defined design variables allows for gradient-based design optimization and thus direct minimization of ground noise.

The design method has been successfully applied to two geometries. The first was a simple axisymmetric body that is built with a limited number of design parameters. This problem allowed for sufficiently large computational meshes which produced very accurate analyses and gradients of noise to the variables. These gradients were verified by locally sampling the nearby design space. Further sampling revealed that even with a limited number of design parameters, the design space was smooth albeit multimodal. Not unexpectedly, when the optimization method was applied, local minima were successfully discovered, though which one depended strongly on the initial design parameters. The success of the design method was demonstrated on several problems involving the axisymmetric body by graphically projecting the optimization trajectories onto the sampled design space.

The second geometry was an actual low-boom aircraft design. The control surface deflections and flight condition were optimized to reduce the ground noise of the aircraft. The design problem included constraints on lift (for level, unaccelerated flight) and pitching moment to maintain trim. Two problems were presented with different starting points, producing two different optimized ground noise values. The first result showed a reduction of over 5 decibels starting from a rather loud initial condition. The second result had a quieter initial state but was able to reduce the ground noise over 3 decibels. These results suggest this design space is also multimodal, though this has not been verified. The lower of the two noise values was very close to what was previously considered the lowest noise possible. While it has not been shown this is the global optimum, successfully achieving the best previously known value further demonstrates the capability of the design method.

VI. Future Work

The results from all of the optimization problems presented strongly suggest that for any parametrized complex or even simple geometry, the ground-noise design space is likely multimodal. The design space may even be *highly* multimodal depending on the complexity of the shock structure emanating from a supersonic body at altitude. Gradient-based optimization techniques simply will not be sufficient in the design of low boom aircraft in general. However, hybrid optimization strategies involving global optimization techniques (e.g., genetic algorithms) along with local gradient-based minimization are a promising avenue to explore in future work.

As computational resources improve, it should be possible to run much finer computational meshes on complex aircraft like the X-59. This would allow for more accurate exploration of the design space and for improved gradient calculation. If more accurate gradients can be computed, the optimization method should be more effective where the design space is flatter near local minima.

Also of interest is the application of the design method on conceptual aircraft. Determining the optimization method's efficacy on an aircraft in early design phases would prove valuable. Can ground noise minimization be used on a conceptual aircraft? Can relatively coarse meshes be used to reduce turnaround time and still produce useful results? Just two of the many questions that should and will be researched in the future.

Acknowledgements

This research was supported by the NASA ARMD Commercial Supersonic Technology (CST) Project and by NASA Ames Research Center contract NNA16BD60C. Computing resources supporting this work were provided by the NASA High-End Computing (HEC) Program through the NASA Advanced Supercomputing (NAS) Division at Ames Research Center.

References

[1] Carter, M., Campbell, R., and Nayani, S., "USM3D Analysis of Low Boom Configuration," AIAA Paper 2011-3335, June 2011. doi:10.2514/6.2011-3335

[2] Choi, S., Alonso, J. J., and Van der Weide, E., "Numerical and Mesh Resolution Requirements for Accurate Sonic Boom Prediction," *Journal of Aircraft*, Vol. 46, No. 4 (2009), pp. 1126-1139. doi:10.2514/1.34367

[3] Cliff, S. E., Thomas, S. D., McMullen, M. S., and Melton, J. E., "Assessment of Unstructured Euler Methods for Sonic Boom Pressure Signatures Using Grid Refinement and Domain Rotation Methods," NASA TM 2008-214568, Sept. 2008.

[4] Cliff, S. E., Elmiligui, A., and Campbell, R., "Evaluation of Refined Tetrahedral Meshes With Projected, Stretched, and Sheared Prism Layers for Sonic Boom Analysis," AIAA Paper 2011-3338, June 2011. doi:10.2514/6.2011-3338

[5] Howe, D., "Hybrid Cart3D/OVERFLOW Near-Field Analysis of a Low Boom Configuration With Wind Tunnel Comparisons," AIAA Paper 2011-3336, June 2011. doi:10.2514/6.2011-3336

[6] Park, M. A. and Nemec, M., "Nearfield Summary and Statistical Analysis of the Second AIAA Sonic Boom Prediction Workshop," *Journal of Aircraft*, Vol. 56, No. 3 (2019), pp. 851-875. doi:10.2514/1.C034866

[7] Park, M., "Low Boom Configuration Analysis With FUN3D Adjoint Simulation Framework," AIAA Paper 2011-3337, June 2011. doi:10.2514/6.2011-3337

[8] Wintzer, M., Nemec, M., and Aftosmis, M. J., "Adjoint-Based Adaptive Mesh Refinement for Sonic Boom Prediction," AIAA Paper 2008-6593, Aug. 2008. doi:10.2514/6.2008-6593

[9] Plotkin, K. J. and Grandi, F., "Computer Models for Sonic Boom Analysis: PCBoom4, CABoom, BooMap, CORBoom," Wyle Report WR 211, 2002.

[10] Rallabhandi, S. K., "Advanced Sonic Boom Prediction Using the Augmented Burgers Equation," *Journal of Aircraft*, Vol. 48, No. 4 (2011), pp. 1245-1253. doi:10.2514/1.C031248

[11] Thomas, C. L., "Extrapolation of Sonic Boom Pressure Signatures By the Waveform Parameter Method," NASA TN D-6832, 1972.

[12] Rallabhandi, S. K. and Loubeau, A., "Summary of Propagation Cases of the Second AIAA Sonic Boom Prediction Workshop," *Journal of Aircraft*, Vol. 56, No. 3 (2018), pp. 876-895. doi:10.2514/1.C034805

[13] Rallabhandi, S. K. and Loubeau, A., "Summary of Propagation Cases of the Third AIAA Sonic Boom Prediction Workshop," *Journal of Aircraft*, (2021), pp. 1-17. doi:10.2514/1.c036327

[14] Aftosmis, M. J., Nemec, M., and Cliff, S. E., "Adjoint-Based Low-Boom Design With Cart3D," AIAA Paper 2011-3500, June 2011. doi:10.2514/6.2011-3500

[15] Li, W. and Rallabhandi, S., "Inverse Design of Low-Boom Supersonic Concepts Using Reversed Equivalent-Area Targets," *Journal of Aircraft*, Vol. 51, No. 1 (2014), pp. 29-36. doi:10.2514/1.C031551

[16] Nadarajah, S., Jameson, A., and Alonso, J., "Sonic Boom Reduction Using an Adjoint Method for Wing-Body Configurations in Supersonic Flow," AIAA Paper 2002-5547, Sept. 2002. doi:10.2514/6.2002-5547

[17] Rallabhandi, S. K. and Mavris, D. N., "Sonic Boom Minimization Using Inverse Design and Probabilistic Acoustic Propagation," *Journal of Aircraft*, Vol. 43, No. 6 (2006), pp. 1815-1828. doi:10.2514/1.20457

[18] Wintzer, M. and Kroo, I. M., "Optimization and Adjoint-Based CFD for the Conceptual Design of Low Sonic Boom Aircraft," AIAA Paper 2012-0963, 2012. doi:10.2514/6.2012-963

[19] Rallabhandi, S. K., Nielsen, E. J., and Diskin, B., "Sonic-Boom Mitigation Through Aircraft Design and Adjoint Methodology," *Journal of Aircraft*, Vol. 51, No. 2 (2014), pp. 502-510. doi:10.2514/1.C032189

[20] Rodriguez, D. L., Aftosmis, M. J., Nemec, M., and Spurlock, W. M., "Adjoint-Based Minimization of X-59 Sonic Boom Noise Via Control Surfaces," AIAA Paper 2021-3030, Jul. 2021. doi:10.2514/6.2021-3030

[21] NASA, "Low Boom Flight Demonstration Overview," Aug. 2019. URL: https://www.nasa.gov/mission_pages/lowboom/overview.

[22] Haimes, R. and Dannenhoffer, J., "The Engineering Sketch Pad: A Solid-Modeling, Feature-Based, Web-Enabled System for Building Parametric Geometry," AIAA Paper 2013-3073, 2013. doi:10.2514/6.2013-3073

[23] Dannenhoffer, J., "OpenCSM: An Open-Source Constructive Solid Modeler for MDAO," AIAA Paper 2013-701, 2013. doi:10.2514/6.2013-701

[24] Haimes, R. and Aftosmis, M., "On Generating High-Quality Water-Tight Triangulations Directly From CAD," *Proceedings of the International Society for Grid Generation (ISGG)*, 2002.

[25] Dannenhoffer, J. and Haimes, R., "Using Design-Parameter Sensitivities in Adjoint-Based Design Environments," AIAA Paper 2017-0139, 2017. doi:10.2514/6.2017-0139

[26] Aftosmis, M. J., Berger, M. J., and Adomavicius, G., "A Parallel Multilevel Method for Adaptively Refined Cartesian Grids With Embedded Boundaries," AIAA Paper 2000-0808, Jan. 2000. doi:10.2514/6.2000-808

[27] Aftosmis, M. J., Berger, M. J., and Melton, J. E., "Robust and Efficient Cartesian Mesh Generation for Component-Based Geometry," *AIAA Journal*, Vol. 36, No. 6 (1998), pp. 952-960. doi:10.2514/2.464

[28] Nemec, M., Aftosmis, M., Murman, S., and Pulliam, T., "Adjoint Formulation for an Embedded-Boundary Cartesian Method," AIAA Paper 2005-877, Jan. 2005. doi:10.2514/6.2005-877

[29] Nemec, M. and Aftosmis, M., "Adjoint Error Estimation and Adaptive Refinement for Embedded-Boundary Cartesian Meshes," AIAA Paper 2007-4187, June 2007. doi:10.2514/6.2007-4187

[30] Nemec, M. and Aftosmis, M. J., "Adjoint Sensitivity Computations for an Embedded-Boundary Cartesian Mesh Method," *Journal of Computational Physics*, Vol. 227, No. 4 (2008), pp. 2724-2742. doi:10.1016/j.jcp.2007.11.018

[31] Aftosmis, M. J. and Nemec, M., "Cart3D Simulations for the First AIAA Sonic Boom Prediction Workshop," AIAA Paper 2014-0558, Jan. 2014. doi:10.2514/6.2014-0558

[32] Anderson, G. R., Aftosmis, M. J., and Nemec, M., "Cart3D Simulations for the Second AIAA Sonic Boom Prediction Workshop," *Journal of Aircraft*, Vol. 56, No. 3 (2019), pp. 896-911. doi:10.2514/1.C034842

[33] Rallabhandi, S., "Sonic Boom Adjoint Methodology and Its Applications," AIAA Paper 2011-3497, June 2011. doi:10.2514/6.2011-3497

[34] Meyer-Bisch, C., "Measuring Noise," *Medecine Sciences: M/S*, Vol. 21, No. 5 (2005), pp. 546-550. doi:10.1051/medsci/2005215546

[35] Rallabhandi, S. K. and Park, M. A., "Adjoint-Based Mesh Adaptation for the Sonic Boom Signature Loudness," AIAA Paper 2017-3049, June 2017. doi:10.2514/6.2017-3049

[36] Gill, P. E., Murray, W., and Saunders, M. A., "SNOPT: An SQP Algorithm for Large-Scale Constrained Optimization," *SIAM Review*, Vol. 47, No. 1 (2005), pp. 99-131. doi:10.1137/S0036144504446096

[37] Nemec, M., Aftosmis, M. J., Rallabhandi, S. K., and Rodriguez, D. L., "Goal-Oriented Discretization Error Control in Coupled Nearfield-Farfield Low-Boom Simulations," AIAA Paper 2022-4085, June 2022. doi:10.2514/6.2022-4085

[38] Nemec, M. and Aftosmis, M., "Parallel Adjoint Framework for Aerodynamic Shape Optimization of Component-Based Geometry," AIAA Paper 2011-1249, Jan. 2011. doi:10.2514/6.2011-1249

[39] Durston, D. A., Elmiligui, A. A., Cliff, S. E., Winski, C., Carter, M. B., and Walker, E., "Experimental and Computational Sonic Boom Assessment of Boeing N+2 Low Boom Models," AIAA Paper 2014-2140, June 2014. doi:10.2514/6.2014-2140

[40] Rallabhandi, S. K., Nemec, M., and Aftosmis, M. J., "Recent Enhancements to Modeling Sonic Boom Propagation Using Augmented Burgers' Equation," AIAA Paper 2023-3727, June 2023. doi:10.2514/6.2023-3727

[41] Rallabhandi, S. K., Nemec, M., and Aftosmis, M. J., "Discretization Error Estimation and Control for Farfield Acoustic Signatures," AIAA Paper 2024-4669, July 2024. doi:10.2514/6.2024-4669